Photocatalytic methane activation by dual reaction sites co-modified WO_3

Keran Wang[a], Lei Luo[a]*, Chao Wang[b], Junwang Tang[b]*

[a] Key Lab of Synthetic and Natural Functional Molecule Chemistry of Ministry of Education, the Energy and Catalysis Hub, College of Chemistry and Materials Science, Northwest University, Xi'an, P. R. China.

[b] Department of Chemical Engineering, University College London, Torrington Place, London WC1E 7JE, UK.

Abstract

Methane (CH_4) upgrading into liquid oxygenates under mild conditions is of great significance to sustainable energy and clean environment, whilst holds great challenges of achieving superior activity and selectivity. Herein, tungsten oxide (WO_3) modified with palladium (Pd) nanoparticles and oxygen vacancies (OVs) was employed as dual reaction sites to drive CH_4 conversion with O_2 at room temperature. Optimized $Pd_{0.5}$-def-WO_3 photocatalyst enables almost 33 times improvement in oxygenates production compared with WO_3, with a yield of 7018 $\mu mol \cdot g^{-1} \cdot h^{-1}$, and a high selectivity of 81 % towards primary products (CH_3OH and CH_3OOH), which is superior to most of the previous reported. In-situ XPS spectra proved Pd nanoparticles were the hole acceptors based on the shift of Pd_{3d} to high binding energy under light irradiation. The in-situ solid-state EPR spectra demonstrate an enhancement of OVs signal which proves the role of OVs as the electron acceptors. Consequently, efficient charge separation has been achieved, contributing to the superior activity and selectivity for CH_4 conversion.

Keywords: photocatalytic methane conversion, cocatalysts, tungsten oxide, oxygen vacancies.

Introduction

As the main constituent of natural gas, methane (CH_4) serves as the combustion fuel and the feedstock in chemical commodities [1]. Combustion or emission of CH_4 aggravates global warming phenomenon due to its tens times higher greenhouse effect than carbon dioxide [2]. Thus, effective conversion of CH_4 into value-added chemicals holds great energy and environmental potentials. Nevertheless, CH_4 conversion is known as the "holy grail" in catalysis due to the symmetrical structure and low polarizability of CH_4, with the dissociation energy of the first C-H bond as high as 440 $kJ \cdot mol^{-1}$ [3, 4]. Industrial processes via reforming and Fischer-Tropsch synthesis benefited from the high activity on CH_4 upgrading, but it is energy-extensive, correspondingly causing environmental issues due to the severe requirement of high temperature. [5] With the continuous progress of thermal catalysts in recent years, CH_4 has been reported to be converted into CH_3OH with Au-Pd colloids [6] and Cu-zeolites at 150 to 200 ℃ [7]. Accordingly, it is highly desired and promising to promote CH_4 conversion under ambient conditions.

Photocatalysis paves the pathways to trigger various reactions at room temperature including water splitting [8-10], CO_2 reduction [11-13] and N_2 fixation [14-16]. Recently, with hydrogen peroxide (H_2O_2) as the oxidant, we reported FeO_x supported TiO_2 photocatalyst to catalyze CH_4 conversion at ambient temperature, with a remarkable selectivity (> 90%) but low yield (352 $\mu mol \cdot g^{-1} \cdot h^{-1}$) of CH_3OH [17]. Amorphous FeOOH modified mesoporous WO_3 could also drive this reaction under similar conditions with a conversion rate of 238.6 $\mu mol \cdot g^{-1} \cdot h^{-1}$ to selectively produce CH_3OH [18]. In parallel, molecule O_2 was used as the much more benign oxidant than H_2O_2 for oxygenates production including CH_3OH [19, 20], ethanol (C_2H_5OH) [21, 22], formaldehyde (HCHO) [23, 24] and formic acid [5]. Among these advances, noble metal modified ZnO and q-$BiVO_4$ photocatalysts could either efficiently activate CH_4 to obtain a high yield of oxygenates or get a high selectivity of

CH_3OH [25, 26]. Nevertheless, great challenges still remain on simultaneously activating CH_4 and suppressing over-oxidation to CO and CO_2.

Co-catalysts could play binary roles in both promoting charge separation and accelerating surface reaction [27]. Noble metals were reported to be the electron acceptors and contributed to the redistribution of electron density, thus promoting the separation and transfer of photogenerated carriers. [28, 29]. In addition to accepting electrons, noble metals could also act as hole acceptors [30-32]. Beside charge dynamics, the chemical adsorption and activation of the reactant on the surface are also important. For metal oxide semiconductors, the introduction of oxygen vacancies (OVs) is regarded as an alternative to address this issue. OVs could promote the activation of small molecules, such as O_2 and H_2O by enhancing their adsorption [33]. It also enhanced light harvesting and charge separation through inserting impurity energy levels [34-36]. Accordingly, the integration of Pd and OVs modification held the potentials to synergistically triggering charge separation and reactant activation.

In this work, Pd nanoparticles and OVs dual reaction sites co-modified WO_3 photocatalyst ($Pd_{0.5}$-def-WO_3) was employed to directly convert CH_4 into liquid oxygenates by O_2 at room temperature. Over the optimized $Pd_{0.5}$-def-WO_3, the photocatalytic conversion of CH_4 into oxygenate products achieved the high yield of 7018 $\mu mol \cdot g^{-1} \cdot h^{-1}$, almost 33 times that of the pristine WO_3. The selectivity of one-carbon (C1) oxygenates including CH_3OH, CH_3OOH and HCHO over $Pd_{0.5}$-def-WO_3 was nearly unity with the selectivity of the primary products (CH_3OH and CH_3OOH) reaching 81%. Mechanism investigation through in-situ electron paramagnetic resonance (EPR) spectra and X-ray photoelectron spectroscopy (XPS) proved that OVs and Pd nanoparticles separately served as the electron and hole acceptors, realizing efficient charge separation and CH_4 conversion performances.

2. Experimental

2.1. Chemicals and materials

Tungsten oxide (WO_3) was purchased from *Adamas-beta*. Polyvinylpyrrolidone (PVP, MW = 58000), ascorbic acid, potassium chloropalladite (K_2PdCl_4) and 5, 5-dimethyl-1-pyrroline-N-oxide (DMPO) were purchased from *Adamas-beta*. Potassium bromide (KBr) was purchased from *Tianjin Fuchen*.

2.2. Preparation of def-WO_3 and Pd_x-def-WO_3

Pd and OVs co-modified WO_3 photocatalyst was prepared based on a modified method [37]. In a typical experiment, 1.00 g WO_3 was first dispersed in 80.0 g deionized water and heated to 80 ℃ in a water bath. Then, 1.05 g PVP, 1.20 g ascorbic acid and 3.00 g KBr were added under continuous stirring. After 10 min reaction, 40 mL aqueous solution with a certain amount of K_2PdCl_4 was poured into the flask. The reaction was terminated after another 3 h. The suspension was then centrifuged, washed, and dried in a vacuum oven at 60 ℃ for 12 h. The as-prepared photocatalyst was denoted as Pd_x-def-WO_3 (x = 0.1, 0.3, 0.5, 0.75 and 1.0 wt%), where x represented the mass percentage of Pd. For comparison, OVs modified WO_3 (denoted as def-WO_3) was prepared under identical conditions but without the addition of K_2PdCl_4.

2.3. Preparation of Pd_x-WO_3

Pd modified WO_3 without OVs was prepared by the photo-deposition method. Briefly, 250 mg WO_3 was dispersed into a mixture of 3 mL CH_3OH and 27 mL deionized water. Then, a certain amount of K_2PdCl_4 solution was added to the above solution and purged with ultra-pure argon (99.999 vol%) for 20 min. Then, the suspension was sealed and irradiated for 3 h at 25 ℃ under stirring in a multi-channel reactor. The samples were collected by centrifugation, washed with deionized water

for three times and dried at 60 ℃ for 12 h.

2.4. Characterizations

X-ray diffraction (XRD) patterns were conducted on the *D8 ADVANCE* diffractometer (*Bruker Co., Ltd*). High-resolution transmission electron microscope (HRTEM) images and energy-dispersive X-ray spectroscopy (EDS) were performed on the *Talos F200X* instrument (*FEI Co., Ltd*). High angle annular dark field scanning transmission (HAADF-STEM) and electron energy loss spectroscopy (EELS) were acquired using *Thermo Fisher Scientific Titan Themis Z*. Nitrogen physical adsorption-desorption isotherms were measured on a *TR2 Star-3020* gas adsorption analyzer at 77 K. Before each measurement, the samples were degassed at 150 ℃ for 8 h and backfilled with ultrapure nitrogen. XPS was recorded on the *PHI 5000 VersaProbeIII* instrument (*ULVAC-PHI Co., Ltd*). In-situ XPS spectra under light irradiation were recorded on the *Thermo Scientific Escalab 250Xi*. UV-vis diffuse reflectance spectra (UV-DRS) were performed on a *UV-3600 Plus* spectrometer with $BaSO_4$ as the reference. Steady-state fluorescence (PL) spectra were acquired on a *JASCO FP-6200* fluorospectrophotometer with the excitation wavelength at 310 nm. Photoelectrochemical properties were measured in a conventional three-electrode cell on the *CHI660E* workstation with photocatalysts loaded tin doped indium oxide (ITO) glass as the working electrode, Ag/AgCl as the reference electrode, platinum plate as the counter electrode and Na_2SO_4 solution (0.1 M) as the electrolyte, respectively. In-situ solid-state EPR measurement under light irradiation and in-situ EPR for the monitor of reactive oxygen species (ROS) were conducted on a *Bruker E500-9.5/12* instrument. During in-situ solid-state EPR measurement to investigate charge kinetics, 20 mg photocatalyst was employed, where the sweep width and microwave frequency were 200 G and 9.82 GHz, respectively. The g value was then calculated according to the following equation: $g = 714.48 \times \nu/H$, where ν is the microwave frequency (GHz) and H is the resonant magnetic field (G). Meanwhile, during the monitor

of ROS, the same microwave frequencies and parameters were used. DMPO was used as the spin-electron trapping agent, then H_2O and CH_3OH were used as the solvent for the monitor of hydroxyl (·OH) and hydroperoxyl (·OOH) radicals, respectively.

2.5. Photocatalytic CH_4 conversion

The photocatalytic CH_4 conversion reaction was conducted in a 200 mL high-pressure batch-reactor equipped with a quartz window. In a typical experiment, 20 mg photocatalyst was dispersed in 100 mL deionized water by ultrasonication for 5 min. Then, the suspension was purged with ultrapure O_2 (99.999 vol%) for 20 minutes. The reactor was next pressurized with 0.1 MPa O_2 and 1.9 MPa CH_4 (99.999 vol%). After well-sealed, the reaction was conducted for 2 h with a 300 W Xenon lamp as the light source (60 $mW \cdot cm^{-2}$, *MICROSOLAR300, Perfectlight*). A thermocouple was inserted into the reactor to directly detect the temperature of the liquid solution. During the reaction process, the reaction temperature was kept at 25 ± 2 ℃ with the cooling system. The gas and liquid products including CO_2 and CH_3OH were analyzed by gas chromatograph (*GC2014, Shimadzu*) equipped with the thermal conductivity detector (TCD) and flame ionization detector (FID). CH_3OOH is a possible product and its concentration was quantified by ^1H NMR (JEOL 400 MHz). Generally, 0.05 μL dimethyl sulfoxide (DMSO) as an internal standard was added to 0.5 mL liquid product for the NMR measurement. HCHO were analyzed by the colorimetric method [38]. For the preparation of chromogenic agent, 15 g ammonium acetate, 0.2 mL pentane-2, 4-dione and 0.3 mL acetic acid were dissolved in deionized water to prepare 100 mL aqueous solution. Then, 1 mL chromogenic agent was mixed with 1 mL reactant and 4 mL deionized water. The absorbance of the solution was tested by Ultraviolet-visible absorption spectrometer at 412 nm after maintaining at 35 °C for about 1 hour. The concentration of HCHO was then quantified according to the standard curve (**Figure S1**) [26]. For reaction condition optimization, only specified parameters were changed

including H_2O amount and molar ratio of CH_4 to O_2.

2.6. Active oxygen species measurements

Semi-quantification of ·OH radicals: the generation of ·OH over various Pd_x-def-WO_3 photocatalysts was measured using coumarin as a fluorescence probe. Coumarin can react with ·OH radicals to form 7-hydroxycoumarin (7-HC), which has a strong fluorescence emission signal at 462 nm under the excitation of 350 nm. In a typical experiment, 20 mg photocatalyst was dispersed in 100 mL coumarin solution (0.5 mM). After stirring for 30 minutes in dark, the mixture was irradiated with Xenon lamp, which reacted for 30 minutes under illumination, and 5 mL suspension was sampled, filtered and measured every 10 minutes [39].

Semi-quantification of ·OOH radicals: the generation of ·OOH radicals over various Pd_x-def-WO_3 photocatalysts was measured through photocatalytic degradation of nitrotetrazolium blue chloride (NBT). ·OOH radicals react quantitatively with NBT to form monomethyl-naphthalene under illumination [40]. Briefly, 25 mg photocatalyst was suspended in 100 mL 0.01 mM NBT aqueous solution. The solution was stirred in dark for 30 min and then irradiated with Xenon lamp for 30 min. 5 mL reaction solution was sampled at 5 min intervals during light irradiation. The amount of unreacted NBT could be detected by *UV-3600 Plus* spectrometer at 259 nm [41].

2.7. Oxygen isotopic labelling experiments

Experiment with isotopic $^{18}O_2$: 20 mg $Pd_{0.5}$-def-WO_3 photocatalyst was dispersed in 2 mL $H_2{}^{16}O$. The reactor was then degassed for 20 minutes, 0.1 MPa $^{18}O_2$ and 1.9 MPa CH_4 were injected into the reactor. After reacting for 6 h under Xenon lamp illumination, the suspension was filtered and then the solvent was analyzed by GC-MS (*QP2020, Shimadzu Co., Ltd*).

Experiment with isotopic $H_2{}^{18}O$: Except for changing $^{18}O_2$ and $H_2{}^{16}O$ into $^{16}O_2$ and $H_2{}^{18}O$, other reaction conditions remained unchanged.

3. Results and discussion

3.1. Crystalline structure and morphology

XRD patterns were conducted to investigate the phase and crystal structure of the as-prepared photocatalysts. All photocatalysts exhibited similar diffraction peaks (**Figure 1a**) at 2θ = 23.1°, 23.6°, 24.3°, 34.1° and 41.9°, which could be assigned to the (002), (020), (200), (220) and (222) planes of monoclinic WO_3 phase (PDF#83-0951) [42]. No extra diffraction peaks (**Figure 1a** and **Figure S2**) were observed for $Pd_{0.5}$-WO_3 and $Pd_{0.5}$-def-WO_3, suggesting the low content or high dispersion of Pd cocatalysts [20, 43]. Solid-state EPR spectra (**Figure 1b**) were measured to investigate whether OVs were introduced during hydrothermal synthesis. Def-WO_3 and $Pd_{0.5}$-def-WO_3 exhibited the single Lorentz signals at g = 2.001, which could be attributed to the electrons trapped by OVs [35], thus suggesting the successful modification of OVs. For a comparison, WO_3 and Pd-WO_3 exhibited absence of EPR signal at g = 2.001, indicating its pristine structure. XPS spectra (**Figure 1c**) further identified the defective structure of WO_3 and Pd_x-def-WO_3. High-resolution W_{4f} XPS spectra could be deconvoluted into four peaks, where the peaks centered at 35.24 and 37.39 eV could be assigned to W^{6+} and the others at 33.89 and 36.28 eV could be attributed to W^{5+} [23]. Additionally, for O_{1s} XPS spectra of WO_3 and $Pd_{0.5}$-def-WO_3 (**Figure 1d**), the peaks located at 530.01 eV and 532.31 eV represented lattice oxygen atom (W-O) and surface-adsorbed hydroxyl group W-OH, respectively [44]. Notably, the peak at 531.17 eV could be attributed to the low coordinated oxygen atoms existing in the lattice, indicating the existence of OVs, which was consistent with the EPR analysis [35].

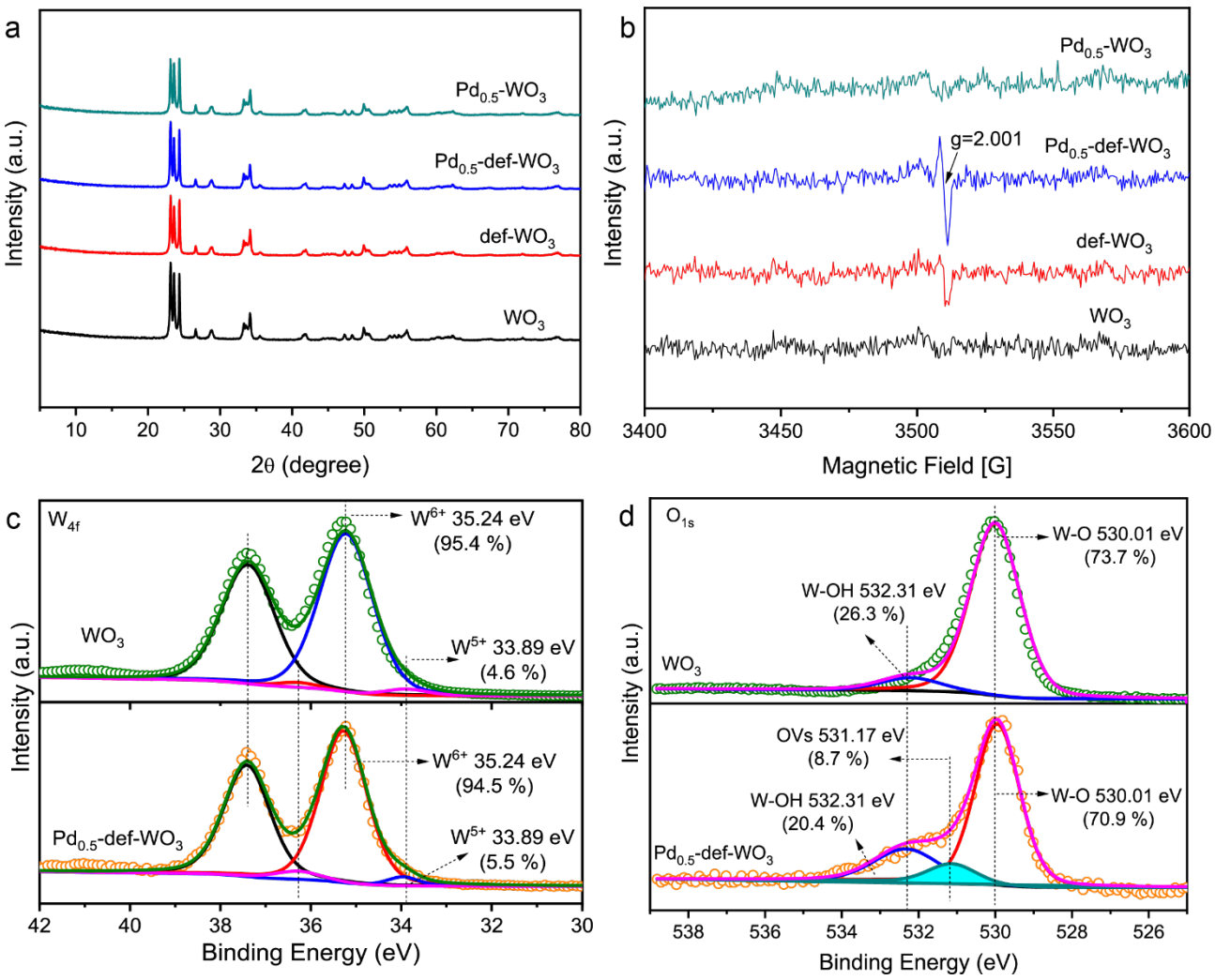

Figure 1. (a) XRD patterns and (b) EPR spectra of WO_3, def-WO_3, $Pd_{0.5}$-def-WO_3 and $Pd_{0.5}$-WO_3. High-resolution (c) W_{4f} and (d) O_{1s} XPS spectra of WO_3 and $Pd_{0.5}$-def-WO_3.

The fine structure of $Pd_{0.5}$-def-WO_3 was characterized by TEM (**Figure 2a**). The crystal facets with 0.38 nm and 0.23 nm lattice space (**Figure 2b**) were indexed to the (200) facet of WO_3 and (111) facet of Pd, respectively [45, 46]. Besides, the EDS-mapping analysis (**Figure 2c-e**) showed that Pd nanoparticles were successfully integrated on the WO_3 substrate. With the increase of Pd loading content, the average size of Pd gradually increased from 4.80 nm to 8.55 nm (**Figure S3, Table S1**), with the specific surface area (**Figure S4**) of the catalyst remaining nearly unchanged at ca. 5 - 8 $m^2 \cdot g^{-1}$. In addition, a thin amorphous layer with ca. 3.5 nm thickness could be seen on WO_3 surface from spherical aberration corrected transmission electron microscope (Cs-TEM) image (**Figure 2f**),

which could be ascribed to the OVs as proved by EPR and XPS analysis. EELS (**Figure 2g**) provided further evidence of the OVs as no correlation peak of O-K edge at 532.24 eV was obviously detected at the three positions [47, 48].

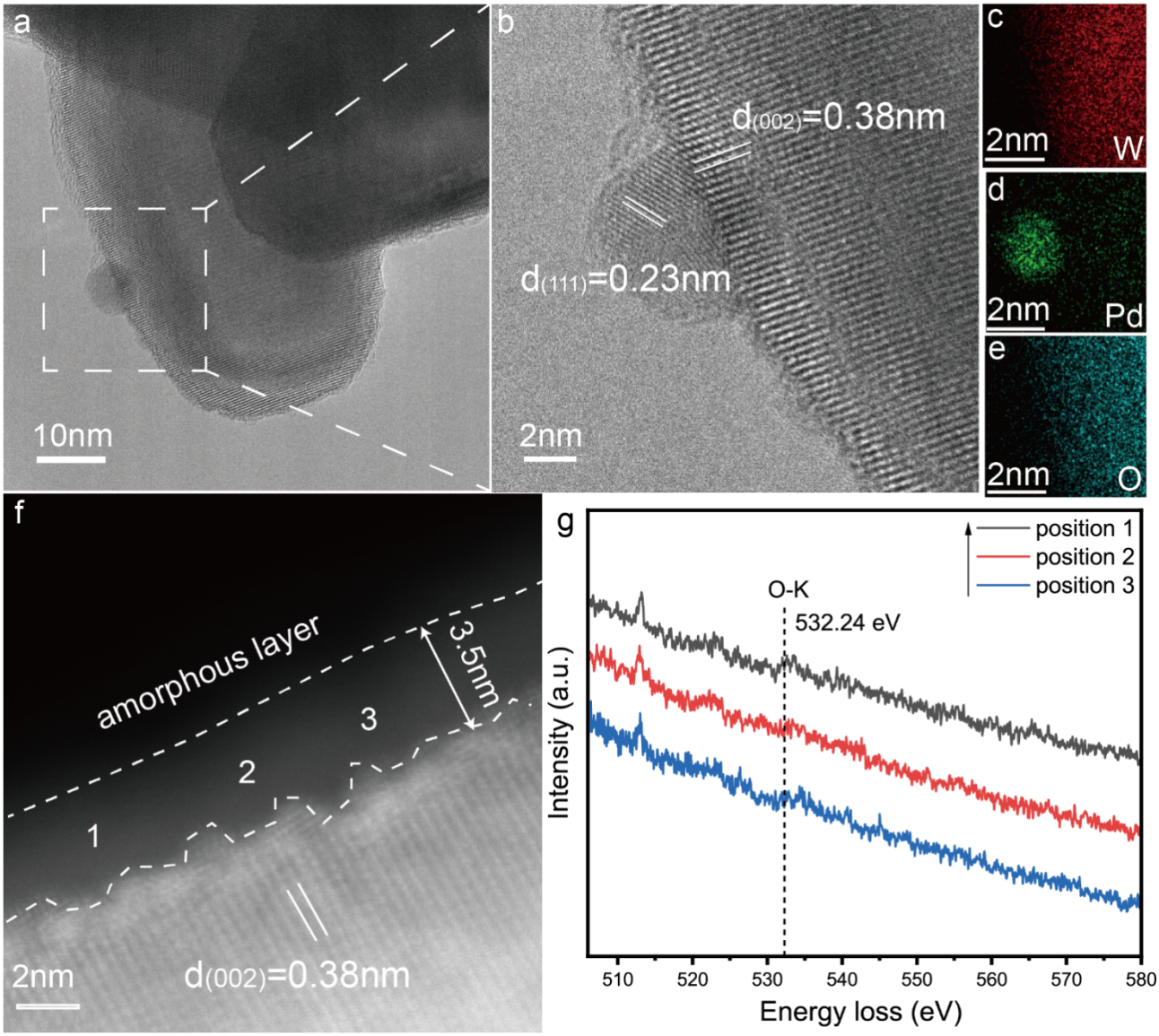

Figure 2. (a, b) HRTEM images, and **(**c-e) EDS-mapping images of $Pd_{0.5}$-def-WO_3. (c) Tungsten, (d) palladium, and (e) oxygen elements were represented by red, green and blue colors, respectively. (f) HAADF-STEM image and (g) O-K EELS at different positions on amorphous layer of $Pd_{0.5}$-def-WO_3. Positions 1, 2 and 3 were three different positions on amorphous layer in (f).

3.2. Photocatalytic CH_4 conversion

The performances of the as-prepared catalysts were evaluated by photocatalytic CH_4 conversion at room temperature in aqueous solution using O_2 as the oxidants. Control experiments without photocatalysts, CH_4, light or O_2 demonstrated that no product could be detected (**Table S2**), revealing that these conditions were indispensable.

Commercial WO_3 exhibited very moderate activity during CH_4 conversion reaction (**Figure 3a**), with only tiny amount of HCHO produced (140 $\mu mol \cdot g^{-1} \cdot h^{-1}$). Such low activity could be mainly attributed to the severe charge recombination in single WO_3 nanocrystals [23]. To enhance charge separation, OVs and Pd co-catalysts as dual reaction sites were introduced herein, as proved by the EPR and XPS above. For def-WO_3, a slightly increased HCHO production rate of 210 $\mu mol \cdot g^{-1} \cdot h^{-1}$ was observed, which was attributed to the valid introduction of OVs. Further loading with Pd cocatalysts dramatically promoted CH_4 activation. ^1H NMR and chromogenic method were used to determine the products of CH_4 conversion on Pd-def-WO_3. Only CH_3OH and CH_3OOH were detected from ^1H NMR spectra at 3.22 ppm and 3.72 ppm [26]. The peak position of HCOOH in ^1H NMR should be between 8.0~8.5 ppm [49], but it was not observed in our study as shown in **Figure S5a**, indicating further oxidation of HCHO to HCOOH did not happen herein. The carbon source of the liquid oxygenate products was confirmed by isotope labeling experiment of $^{13}CH_4$ on $Pd_{0.5}$-def-WO_3. The reaction was carried out in 3 mL water for 6 h with the feed of the mixed gas of 0.4 MPa $^{13}CH_4$ and 0.1 MPa O_2. As shown in **Figure S5b**, three ^{13}C NMR peaks at 48.3, 81.2 and 100.3 ppm were attributed to CH_3OH, CH_3OOH and $HOCH_2OH$ (the main substance of HCHO in H_2O) respectively, which confirmed that all liquid oxygenate products really originated from CH_4 conversion [50]. Moreover, it showed the absence of the peak at 164.0 ppm [51], further indicating no HCOOH was produced. Such results again were attributed to the weakened oxidative ability of photo-induced hole

due to its transfer from VB of WO_3 to Pd nanoparticles, which could inhibit the deep oxidation of oxygenate products. H_2O was the other reason to suppress deep oxidation through promoting the timely desorption of oxygenate products such as CH_3OH. The size-dependent behavior of Pd nanoparticles on the performance of photocatalytic methane conversion were also investigated (**Figure 3a and Table S1**). With the increase of Pd loading from 0.1 wt% to 1.0 wt%, the average size of Pd nanoparticles increased, and the yield of oxygenate products showed a volcanic trend, with the highest yield of oxygenates (7018 $\mu mol \cdot g^{-1} \cdot h^{-1}$) and the highest selectivity of primary products (including CH_3OH and CH_3OOH) (81%) observed over $Pd_{0.5}$-def-WO_3. Further increasing Pd content led to the weakened activity which could be due to the larger average size of Pd of 8.55 nm on $Pd_{1.0}$-def-WO_3 (**Table S1**), which could scatter more light. XPS analysis (**Figure S6** and **S7, Table S3**) showed that the ratio of Pd^0/Pd^{2+} increased with the increase of Pd size. Besides Pd cocatalysts, OVs also played vital roles on CH_4 activation. Compared with $Pd_{0.5}$-WO_3 without OVs, $Pd_{0.5}$-def-WO_3 showed 2.5 times higher yield of oxygenates. Moreover, Pd and OVs showed synergistic effect on CH_4 conversion since the yield of oxygenates over $Pd_{0.5}$-def-WO_3 (7018 $\mu mol \cdot g^{-1} \cdot h^{-1}$) was much higher than the sum of $Pd_{0.5}$-WO_3 (2804 $\mu mol \cdot g^{-1} \cdot h^{-1}$) and def-$WO_3$ (210 $\mu mol \cdot g^{-1} \cdot h^{-1}$). The detailed photocatalytic CH_4 conversion performance over all photocatalysts was displayed in **Table S4**. The total amount of C1 products over $Pd_{0.5}$-def-WO_3 catalyst was 33 times as that of the pristine WO_3, resulting in an apparent quantum yield (AQY) of 0.56 % at 420 ± 10 nm (**Table S5**), which was much higher than almost all WO_3-based photocatalysts reported (**Table S6**). The selectivity to C1 on the optimized photocatalyst was 99.3 % and to CO_2 was 0.7 %, being one of the best results.

Molar ratio of CH_4 to O_2 was then investigated and shown in **Figure 3b**. When it decreased from 19.5/0.5 to 19/1, the yield of oxygenates increased from 5000 to 7018 $\mu mol \cdot g^{-1} \cdot h^{-1}$, corresponding with the improved O_2 concentration in water. Further decreasing the molar ratio of CH_4 to O_2 resulted

in the gradually decreased yield of products from 7018 to 1053 μmol·g^{-1}·h^{-1}. Meanwhile, the selectivity of the primary products was also reduced from 81 % to 51 %, which was mainly assigned to the increased O_2 dissolved in water, which could over-oxidize the product to CO_2.

Similarly, when water amount increased (**Figure 3c**), the yield of oxygenated liquid products also increased from 2461 μmol·g^{-1}·h^{-1} for 25 mL to 7018 μmol·g^{-1}·h^{-1} for 100 mL, with the selectivity of primary products improved from 40 % to 81 %. Such improved production was ascribed to that the higher amount of water would promote desorption of oxygenate products, thus inhibiting the over-oxidation.

The recycling experiments over $Pd_{0.5}$-def-WO_3 photocatalyst were carried out to study its stability. According to the results of the cycling experiment (**Figure S8a**), the performance of $Pd_{0.5}$-def-WO_3 catalyst decreased by 15% from 7018 μmol·g^{-1}·h^{-1} to 5952 μmol·g^{-1}·h^{-1} after the first cycle, and then the performance of the catalyst was relatively stable for the next 3 cycles at 5340 μmol·g^{-1}·h^{-1}. XPS spectra (**Figure S8b**) further indicated that the ratio of OVs to $Pd_{0.5}$-def-WO_3 was very similar before and after the reaction. It thus concluded that $Pd_{0.5}$-def-WO_3 exhibited a good stability after the first run.

3.3. Mechanism investigation

UV-DRS spectra were measured to study the light absorption and displayed in **Figure 4a**. Pristine WO_3 exhibited an absorption edge of around 470 nm, showing weak absorption in the visible light range. When Pd was loaded, the absorption edge of the catalysts hardly changed. According to the Tauc plot (**Figure S9**), the bandgap energy (E_g) of $Pd_{0.5}$-def-WO_3 was established as 2.84 eV, in agree with the previous report [52]. Based on the Mott-Schottky plots of the $Pd_{0.5}$-def-WO_3 photocatalysts measured at different frequencies (**Figure S10**), the flat band potential of $Pd_{0.5}$-def-WO_3 was

determined as -0.59 V (vs. Ag/AgCl), or 0.02 V (vs. NHE). As the flat band potential is regarded as

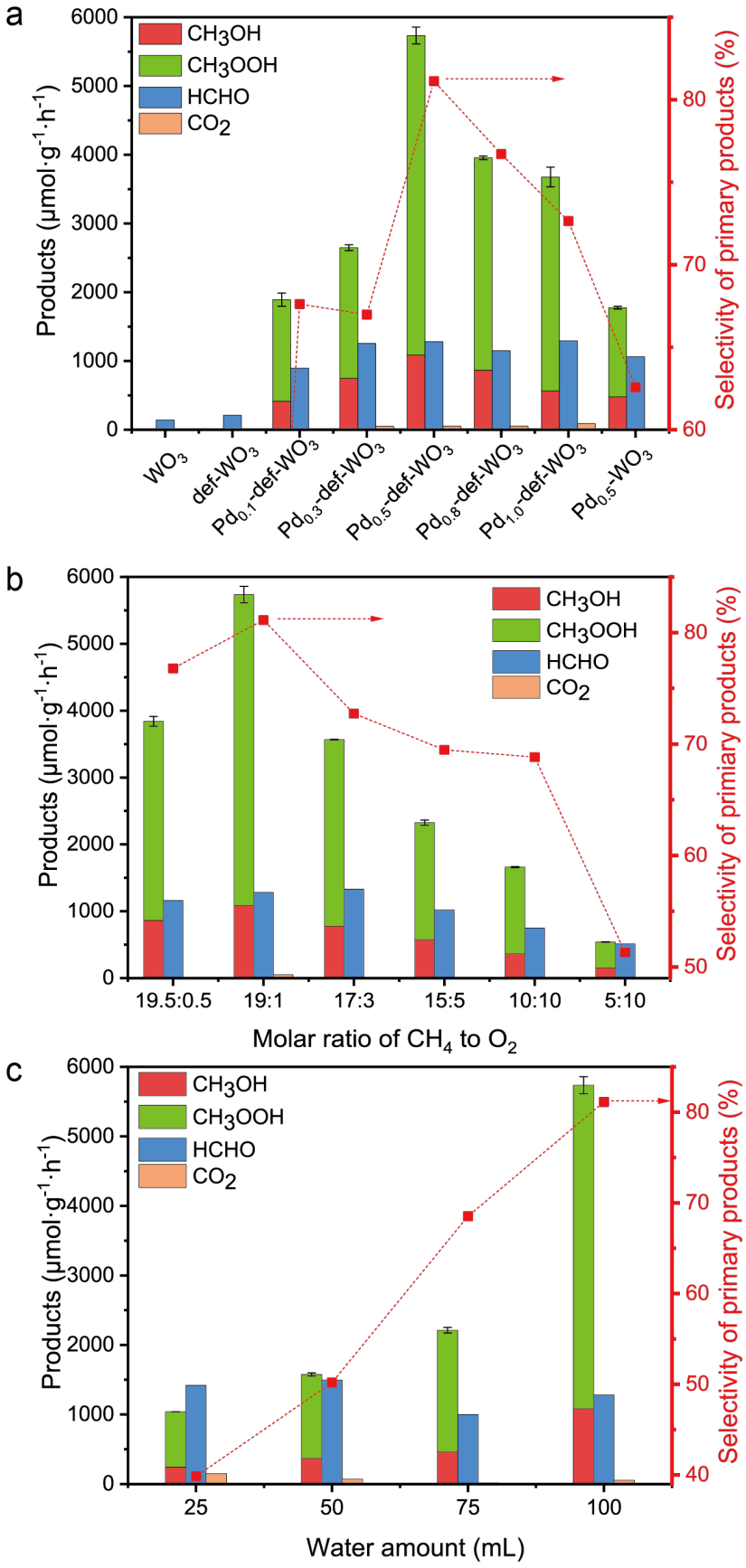

Figure 3. Photocatalytic CH_4 conversion (a) over WO_3, def-WO_3, Pd_x-def-WO_3 and $Pd_{0.5}$-WO_3

photocatalysts. Reaction conditions: 20 mg catalyst, 100 mL H_2O, 1.9 MPa CH_4, 0.1 MPa O_2, 2 h, 25 ℃, 100 $mW \cdot cm^{-2}$. Investigation on effect of (b) molar ratio of CH_4 to O_2 and (c) H_2O amount.

0.1 V below the conduction band for an n-type semiconductor, the conduction band (CB) potential (vs. NHE) of $Pd_{0.5}$-def-WO_3 was -0.08 V. Combining the bandgap and CB potential, the valance band (VB) potential was calculated to be 2.76 V.

To further clarify the chemical state of Pd species and the charge transfer dynamics, in-situ XPS under light irradiation was carried out (**Figure 4b**). In dark, the Pd_{3d} XPS peaks located at 335.00 eV and 340.30 eV was attributed to Pd^0 species, and these at 336.72 eV and 342.18 eV to Pd^{2+} species [53]. Under light irradiation, the peaks associated with Pd^0 exhibited an obvious left-shift from 335.00 eV to 335.51 eV, suggesting Pd was partially oxidized to $Pd^{\delta+}$ ($2 > \delta > 0$) upon light irradiation while Pd^{2+} species remain the same position, thus suggesting photo-induced hole transferring from the valence band of $Pd_{0.5}$-def-WO_3 to Pd nanoparticles, which is consistent with the literatures [30-32].

The function of OVs was characterized by in-situ EPR spectra in dark and under light irradiation. In dark, def-WO_3 showed a signal at g = 2.001, belonging to the spin electrons trapped by OVs [35]. The intensity of this signal then exhibited obvious enhancement under light irradiation (**Figure 4c**), which implied a higher density of electrons trapped by OVs under light irradiation, thus suggesting OVs acted as the electron acceptors [54, 55]. Therefore, OVs could not only enhance light absorption, but also acted as an electron acceptor to promote the photo-generated charge separation [56].

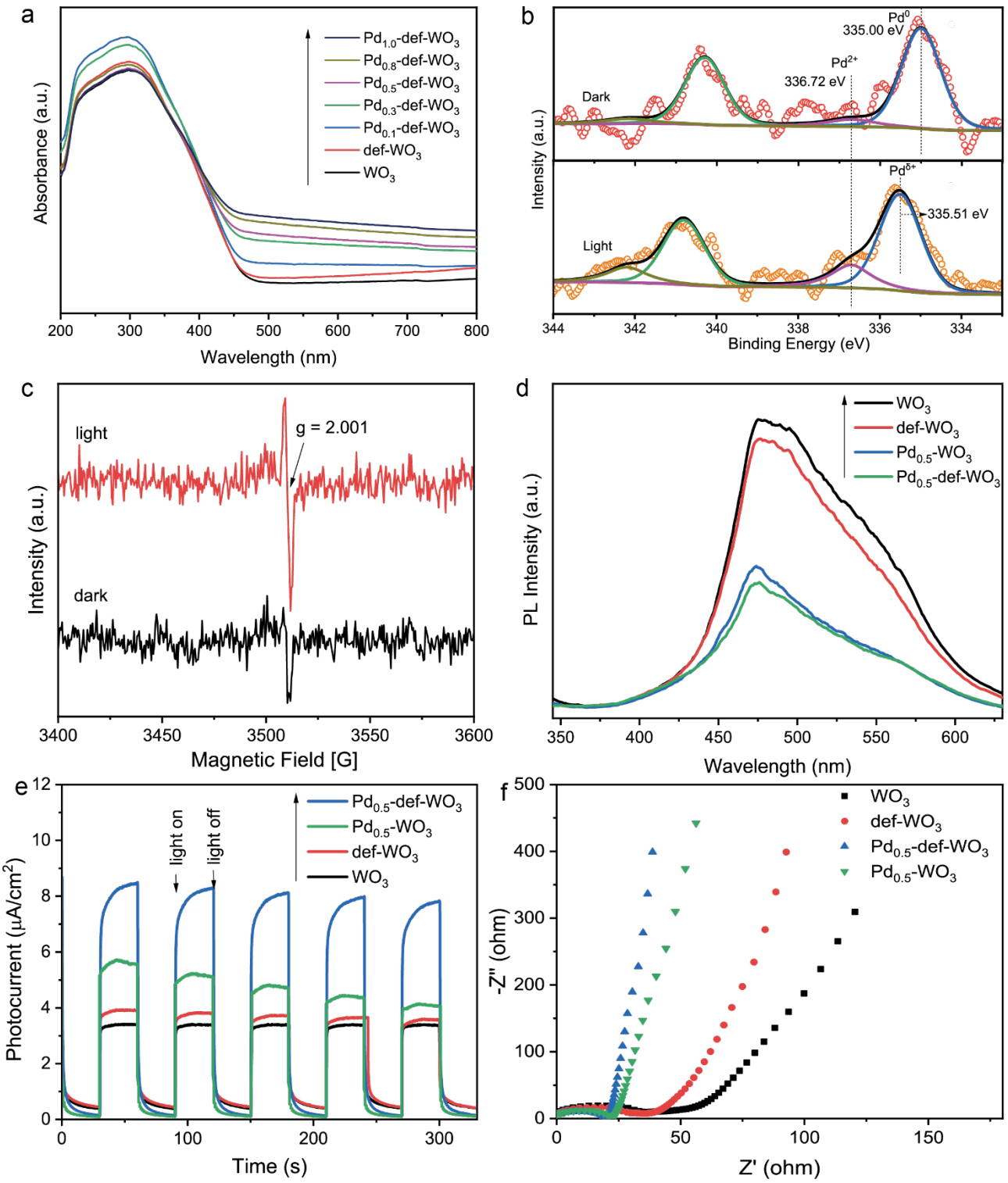

Figure 4. (a) UV-DRS spectra of different photocatalysts. (b) In-situ Pd_{3d} XPS spectra of $Pd_{0.5}$-def-WO_3 in dark and under light irridiation. (c) In-situ solid-state EPR spectra of def-WO_3 in dark and under light irridiation. (d) Steady-state PL spectra, (e) transient photocurrent responses and (f) EIS plots of different photocatalysts.

Efficient charge separation is important for the consecutive surface reaction with the adsorbed reactants, such as O_2 and H_2O. Charge separation behavior was further investigated by steady-state PL spectra. Generally, stronger emission signal of PL spectra indicated more severe charge recombination efficiency. It could be seen that WO_3 exhibited a strong PL peak (**Figure 4d**), corresponding with the severe charge recombination [57]. When OVs were introduced, the PL signal of def-WO_3 decreased, suggesting charge recombination was suppressed because of the role of OVs as electron acceptors as proven by the in-situ EPR spectra. When modified with Pd nanoparticles, the fluorescence signal of $Pd_{0.5}$-WO_3 decreased obviously. Notably, with the co-modification of OVs and Pd cocatalysts, $Pd_{0.5}$-def-WO_3 performed the weakest PL intensity, which could be attributed to the synergistic effect of Pd and OVs. Charge separation was also investigated by photocurrent response analysis. Among four photocatalysts, $Pd_{0.5}$-def-WO_3 (**Figure 4e**) exhibited the strongest photocurrent intensity, indicating that OVs and metal Pd species could promote the separation of photo-generated charge carriers. Besides, electrochemical impedance spectroscopy (EIS) Nyquist plots were measured to describe charge transfer resistance (**Figure 4f**). $Pd_{0.5}$-def-WO_3 with the smallest radius suggested a low resistance for charge transfer. With a close look at the above results, it concluded that the synergy of OVs and Pd species could efficiently promote the separation and transfer of photo-generated electrons and holes.

Reactive oxygen species (ROS) induced by the separated charge carriers are very important for CH_4 activation and oxygenate formation. The redox potentials are -0.05V for $E^0(O_2/\cdot OOH)$ and 2.30 V for $E^0(H_2O/\cdot OH)$ [58], and the measured CB and VB energy levels were -0.08 V and 2.76 V. One could see that the potentials of CB and VB for $Pd_{0.5}$-def-WO_3 were sufficient to drive O_2 reduction and H_2O oxidation to produce ·OOH and ·OH radicals, respectively. In-situ EPR spectra were conducted to monitor ROS including ·OOH and ·OH radicals, with DMPO as the spin-electron

trapping agents. No signals were detected in dark over $Pd_{0.5}$-def-WO_3. Under light irradiation, six prominent characteristic signals (A_H = 9.2 G and A_N = 13.5 G) were observed and could be attributed to the DMPO-OOH adduct (**Figure 5a**), indicating that ·OOH radicals were the active species during CH_4 conversion [59]. Photocatalytic NBT degradation experiments were then conducted to quantitatively compare the generation of ·OOH radicals over different photocatalysts (**Figure S11**). It could be seen from **Figure 5b** that $Pd_{0.5}$-def-WO_3 exhibited the first-order kinetic constant (0.017 min^{-1}) for NBT degradation, much larger than that of 0.005 min^{-1} for WO_3, 0.008 min^{-1} for def-WO_3 and 0.009 min^{-1} for $Pd_{0.5}$-WO_3. Such larger kinetic constant demonstrated higher generation rate of ·OOH radicals by $Pd_{0.5}$-def-WO_3, which came from the reduction of molecule O_2 by photo-induced electrons. In parallel, ·OH radicals were also monitored in water through in-situ EPR **(Figure 5c)** with DMPO as the trapping agent. The quadruple signals ($A_H = A_N$ = 15 G) with relative intensity of 1: 2: 2: 1 for $Pd_{0.5}$-def-WO_3 under light irradiation were ascribed to DMPO-OH adduct [60]. At the same time, the ability of different catalysts to produce ·OH radicals was studied (**Figure 5d**) by using coumarin as the probe, where coumarin could easily react with ·OH to produce 7-hydroxycoumarin, which could be detected due to the strong PL emission at 462 nm. The generated PL signal of 7-HC was the strongest on $Pd_{0.5}$-def-WO_3, indicating the highest concentration of ·OH radicals. It thus demonstrated that Pd nanoparticles could promote the generation of ·OH radicals in water, and then promoted the activation of CH_4. One could see that $Pd_{0.5}$-def-WO_3 exhibited much higher ability for the generation of ·OH and ·OOH radicals than the others, which contributed to its boosted photocatalysis.

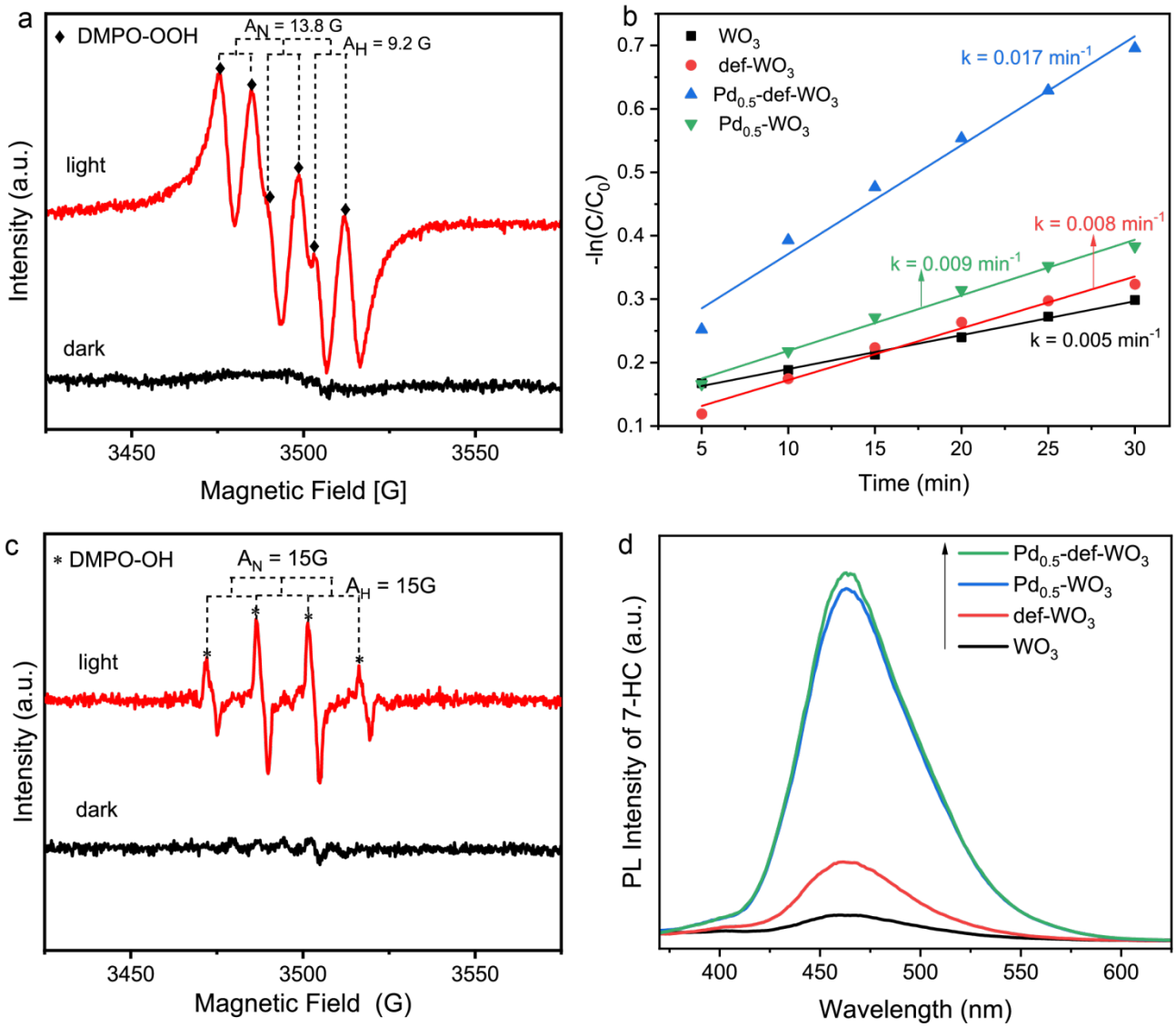

Figure 5. (a) In-situ EPR spectra to monitor of DMPO-OOH over $Pd_{0.5}$-def-WO_3 in CH_3OH solution. (b) First-order kinetic constant of NBT photodegradation reaction for detection of ·OOH radicals formation. (c) In-situ EPR spectra to monitor of DMPO-OH over $Pd_{0.5}$-def-WO_3 in water. (d) PL spectra of the as-generated 7-HC over different photocatalysts.

To confirm the oxygen source in the produced oxygenates, we carried out the isotopic experiments by using isotopic $^{18}O_2$ or $H_2{}^{18}O$ during CH_4 conversion [61]. With the dosage of $H_2{}^{18}O$ and $^{16}O_2$, predominant mass signals were observed at m/z = 31 and 32 which were ascribed to $CH_3{}^{16}OH$ and its major fragment (**Figure 6**). Further evidences came from the results by using $^{18}O_2$ and $H_2{}^{16}O$ as

the reactants, $CH_3{}^{18}OH$ and its fragment (m/z = 33 and 34) were primarily detected [61]. These thus suggested that molecule O_2 was the main oxygen source directly participating in the formation of oxygenates.

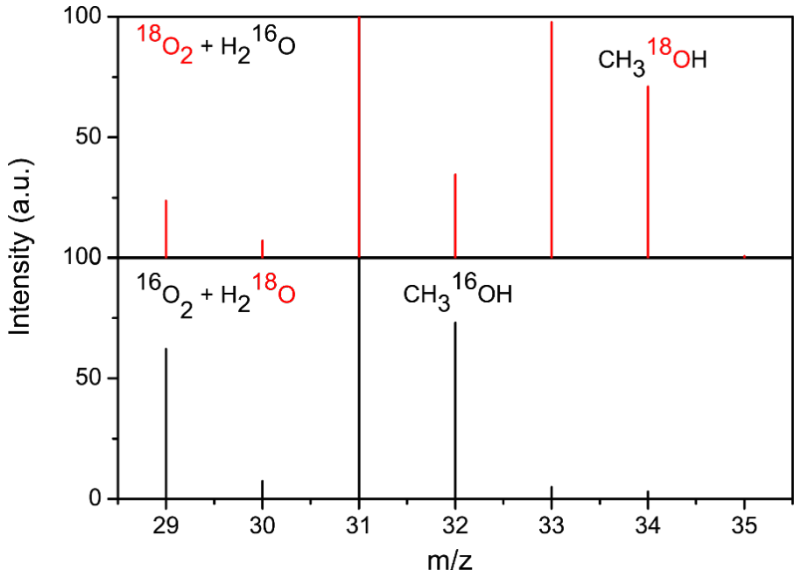

Figure 6. GC-MS spectra of the generated CH_3OH over $Pd_{0.5}$-def-WO_3 with $^{18}O_2 + H_2{}^{16}O$ or $^{16}O_2 + H_2{}^{18}O$ in photocatalytic CH_4 oxidation.

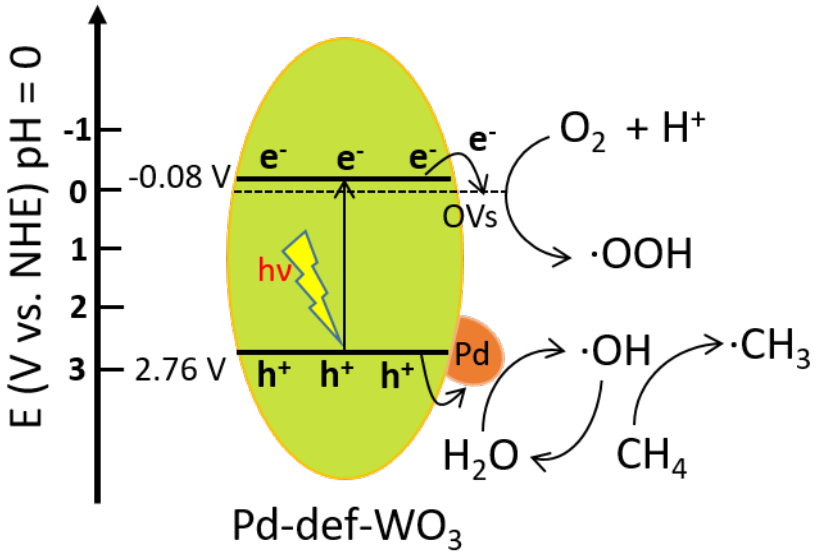

Scheme 1. Proposed reaction process of photocatalytic CH_4 oxidation over $Pd_{0.5}$-def-WO_3 with O_2 as the oxidant.

Based on the above results, the mechanism for the selective oxidation of CH_4 over $Pd_{0.5}$-def-WO_3 catalyst was proposed (**Scheme 1**). Upon light irradiation, electrons were excited from the VB (E = 2.76 V) to the CB (E = -0.08 V) of WO_3, with the holes settled on the VB, which satisfied the production of ROS (·OH radicals and ·OOH radicals). Then the electrons on the CB migrated to OVs as proven by in-situ EPR spectra (**Figure 4c**), reducing O_2 with a proton to produce ·OOH radicals [62]. In-situ EPR spectra (**Figure 5a**) under light over $Pd_{0.5}$-def-WO_3 also verified the generation of ·OOH radicals. Meanwhile, photo-induced holes on the valence band transferred to Pd nanoparticles, and promoted H_2O oxidation to produce ·OH radicals [63]. In-situ XPS analysis (**Figure 4b**) demonstrated Pd was functionlized as the hole acceptors. The generated ·OH radicals next activated CH_4 into $\cdot CH_3$ radicals, which then coupled with ·OOH radicals to produce the primary product of CH_3OOH. It further converted to CH_3OH with two protons in the aqueous solution [38]. The generated CH_3OOH and CH_3OH could be over-oxidized to HCHO and CO_2 [64]. Therefore, the synergistic effects of OVs and Pd nanoparticles promoted CH_4 conversion. Isotopic experiments (**Figure 6**) with $^{18}O_2$ and $H_2{}^{18}O$ proved that oxygen atoms in liquid oxygenates primarily originated from O_2.

Conclusion

In summary, at ambient temperature, CH_4 oxidation to liquid oxygenates by O_2 realized over Pd nanoparticles and oxygen vacancies dual reaction sites co-modified WO_3 photocatalysts with the assistance of H_2O. It presented 7018 $\mu mol \cdot g^{-1} \cdot h^{-1}$ C1 oxygenate production with 81% selectivity of the primary products (CH_3OOH and CH_3OH) over $Pd_{0.5}$-def-WO_3, while 0.7 % selectivity to CO_2. In-situ XPS and EPR spectra proved that Pd nanoparticles and oxygen vacancies accepted

photogenerated holes and electrons, respectively, which synergistically promoted charge separation. Isotopic experiments demonstrated that O_2 was the predominant oxygen source to produce oxygenates, and the function of H_2O was mainly to promote the activation of CH_4 by generating ·OH radicals. This work provided the in-depth understanding on simultaneous regulation of both activity and selectivity during CH_4 conversion at ambient temperature.

Notes

The authors declare no competing of interest.

Acknowledgements

All authors are grateful for the Shaanxi Key Research Grant (China, 2020GY-244). L. L. is thankful for the China Postdoctoral Science Foundation (Grant No. 2019M663802). J. T. and C. W. are thankful for financial support from the UK EPSRC (EP/S018204/2), Leverhulme Trust (RPG-2017-122), Royal Society Newton Advanced Fellowship grant (NAF\R1\191163 and NA170422) and Royal Society Leverhulme Trust Senior Research Fellowship (SRF\R1\21000153).

References

1. Song, H., Meng, X., Wang, Z., Liu, H., and Ye, J. *Joule*, **2019**. 3, 1606-1636.
2. Mohamedali, M., Ayodele, O., and Ibrahim, H. *Renew. Sustain. Energy Rev.*, **2020**. 131, 110024.
3. Schwach, P., Pan, X., and Bao, X. *Chem Rev*, **2017**. 117, 8497-8520.
4. Zhou, Y., Zhang, L., and Wang, W. *Nat. Commun.*, **2019**. 10, 506.
5. Cui, X., Huang, R., and Deng, D. *Energy Chem.*, **2021**. 3, 100050.
6. Agarwal, N., Freakley, S.J., McVicker, R.U., Althahban, S.M., Dimitratos, N., He, Q., Morgan, D.J., Jenkins, R.L., Willock, D.J., Taylor, S.H., Kiely, C.J., and Hutchings, G.J. *Science*, **2017**.

358, 223-227.

7. Hammond, C., Forde, M.M., Ab Rahim, M.H., Thetford, A., He, Q., Jenkins, R.L., Dimitratos, N., Lopez-Sanchez, J.A., Dummer, N.F., Murphy, D.M., Carley, A.F., Taylor, S.H., Willock, D.J., Stangland, E.E., Kang, J., Hagen, H., Kiely, C.J., and Hutchings, G.J. *Angew Chem Int Ed Engl*, **2012**. 51, 5129-33.
8. Wang, Q., Nakabayashi, M., Hisatomi, T., Sun, S., Akiyama, S., Wang, Z., Pan, Z., Xiao, X., Watanabe, T., Yamada, T., Shibata, N., Takata, T., and Domen, K. *Nat. Mater.*, **2019**. 18, 827-832.
9. Su, T., Shao, Q., Qin, Z., Guo, Z., and Wu, Z. *ACS Catal.*, **2018**. 8, 2253-2276.
10. Li, Y.H., Wang, Y., Zheng, L.R., Zhao, H.J., Yang, H.G., and Li, C. *Appl. Catal. B*, **2017**. 209, 247-252.
11. Kreft, S., Schoch, R., Schneidewind, J., Rabeah, J., Kondratenko, E.V., Kondratenko, V.A., Junge, H., Bauer, M., Wohlrab, S., and Beller, M. *Chem.*, **2019**. 5, 1818-1833.
12. Tamaki, Y. and Ishitani, O. *ACS Catal.*, **2017**. 7, 3394-3409.
13. Jiao, X., Zheng, K., Hu, Z., Sun, Y., and Xie, Y. *ACS Cent. Sci.*, **2020**. 6, 653-660.
14. Ojha, N. and Kumar, S. *Appl. Catal. B*, **2021**. 292, 120166.
15. Xiong, J., Song, P., Di, J., and Li, H. *Chem. Eng. J.*, **2020**. 402, 126208.
16. Li, H., Mao, C., Shang, H., Yang, Z., Ai, Z., and Zhang, L. *Nanoscale*, **2018**. 10, 15429-15435.
17. Xie, J., Jin, R., Li, A., Bi, Y., Ruan, Q., Deng, Y., Zhang, Y., Yao, S., Sankar, G., Ma, D., and Tang, J. *Nat. Catal.*, **2018**. 1, 889-896.
18. Yang, J., Hao, J., Wei, J., Dai, J., and Li, Y. *Fuel*, **2020**. 266, 117104.
19. Yang, J., Chen, P., Dai, J., Chen, Y., Rong, L., and Wang, D. *Energy Convers. Manag.*, **2021**. 247, 114767.
20. Chen, J., Giewont, K., Walker, E.A., Lee, J., Niu, Y., and Kyriakidou, E.A. *ACS Catal.*, **2021**. 11, 13066-13076.
21. Bashir, S. and Idriss, H. *Catal. Sci. & Technol.*, **2017**. 7, 5301-5320.
22. Zhou, Y., Zhang, L., and Wang, W. *Nat Commun.*, **2019**. 10, 506.
23. Wei, S., Zhu, X., Zhang, P., Fan, Y., Sun, Z., Zhao, X., Han, D., and Niu, L. *Appl. Catal., B*, **2021**. 283, 119661.
24. Fan, Y., Zhang, P., Lu, R., Jiang, Y., Pan, G., Wang, W., Zhu, X., Wei, S., Han, D., and Niu, L. *Catal. Commun.*, **2021**. 161, 106365.

25. Wang, G., Zhang, W., Li, J., Dong, X., and Zhang, X. *J. Mater. Sci.*, **2019**. 54, 6488-6499.
26. Song, H., Meng, X., Wang, S., Zhou, W., Wang, X., Kako, T., and Ye, J. *J. Am. Chem. Soc.*, **2019**. 141, 20507-20515.
27. Meng, A., Zhang, L., Cheng, B., and Yu, J. *Adv Mater*, **2019**. 31, e1807660.
28. Huang, H. and Leung, D.Y.C. *ACS Catalysis*, **2011**. 1, 348-354.
29. Kim, Y. and Kim, D.H. *Applied Catalysis B: Environmental*, **2019**. 244, 684-693.
30. Karbalaei Akbari, M., Hai, Z., Wei, Z., Hu, J., and Zhuiykov, S. *Mater. Res. Bull.*, **2017**. 95, 380-391.
31. Zhu, W., Wu, Z., Foo, G.S., Gao, X., Zhou, M., Liu, B., Veith, G.M., Wu, P., Browning, K.L., Lee, H.N., Li, H., Dai, S., and Zhu, H. *Nat. Commun.*, **2017**. 8, 15291.
32. Luo, L., Gong, Z., Xu, Y., Ma, J., Liu, H., Xing, J., and Tang, J. *J. Am. Chem. Soc.*, **2022**. 144, 740-750.
33. Ma, D., Yang, L., Sheng, Z., and Chen, Y. *Chem. Eng. J.*, **2021**. 405, 126538.
34. Lei, F., Sun, Y., Liu, K., Gao, S., Liang, L., Pan, B., and Xie, Y. *J. Am. Chem. Soc.*, **2014**. 136, 6826-9.
35. Zhang, N., Li, X., Ye, H., Chen, S., Ju, H., Liu, D., Lin, Y., Ye, W., Wang, C., Xu, Q., Zhu, J., Song, L., Jiang, J., and Xiong, Y. *J Am Chem Soc*, **2016**. 138, 8928-35.
36. Wang, W., Strohbeen, P.J., Lee, D., Zhou, C., Kawasaki, J.K., Choi, K.-S., Liu, M., and Galli, G. *Chemistry of Materials*, **2020**. 32, 2899-2909.
37. Long, R., Li, Y., Liu, Y., Chen, S., Zheng, X., Gao, C., He, C., Chen, N., Qi, Z., Song, L., Jiang, J., Zhu, J., and Xiong, Y. *J. Am. Chem. Soc.*, **2017**. 139, 4486-4492.
38. Song, H., Meng, X., Wang, S., Zhou, W., Wang, X., Kako, T., and Ye, J. *J Am Chem Soc*, **2019**. 141, 20507-20515.
39. De-Nasri, S.J., Nagarajan, S., Robertson, P.K.J., and Ranade, V.V. *Chemical Engineering Journal*, **2021**. 420, 127560.
40. Wolski, L., Walkowiak, A., and Ziolek, M. *Catalysis Today*, **2019**. 333, 54-62.
41. Qian, J., Dang, W.Q., Li, J., Zhang, W., Tian, M., Wang, N., Song, W.J., Lv, L.L., and Jiang, H.Y. *Catal. Sci. Technol.*, **2021**. 11, 2379-2385.
42. Parthibavarman, M., Karthik, M., and Prabhakaran, S. *Vacuum*, **2018**. 155, 224-232.
43. Singh, S.P., Yamamoto, A., Fudo, E., Tanaka, A., Kominami, H., and Yoshida, H. *ACS Catal.*, **2021**. 11, 13768-13781.

44. Cheng, H., Klapproth, M., Sagaltchik, A., Li, S., and Thomas, A. *J. Mater. Chem. A*, **2018**. 6, 2249-2256.

45. Yang, M., Li, J., Ke, G., Liu, B., Dong, F., Yang, L., He, H., and Zhou, Y. *J. Energy Chem.*, **2021**. 56, 37-45.

46. Ramírez-Ortega, D., Guerrero-Araque, D., Acevedo-Peña, P., Lartundo-Rojas, L., and Zanella, R. *J. Mater. Sci.*, **2020**. 55, 16641-16658.

47. Anithaa, A.C., Lavanya, N., Asokan, K., and Sekar, C. *Electrochim. Acta*, **2015**. 167, 294-302.

48. Choi, S.Y., Kim, S.D., Choi, M., Lee, H.S., Ryu, J., Shibata, N., Mizoguchi, T., Tochigi, E., Yamamoto, T., Kang, S.J., and Ikuhara, Y. *Nano Lett.*, **2015**. 15, 4129-34.

49. Tang, Y., Li, Y., Fung, V., Jiang, D.E., Huang, W., Zhang, S., Iwasawa, Y., Sakata, T., Nguyen, L., Zhang, X., Frenkel, A.I., and Tao, F.F. *Nat. Commun.*, **2018**. 9, 1231.

50. Gaca, K.Z., Parkinson, J.A., Lue, L., and Sefcik, J. *Ind. Eng. Chem. Res.*, **2014**. 53, 9262-9271.

51. Tang, Y., Li, Y., Fung, V., Jiang, D.E., Huang, W., Zhang, S., Iwasawa, Y., Sakata, T., Nguyen, L., Zhang, X., Frenkel, A.I., and Tao, F.F. *Nat Commun*, **2018**. 9, 1231.

52. Hameed, A., Ismail, I.M.I., Aslam, M., and Gondal, M.A. *Appl. Catal. A*, **2014**. 470, 327-335.

53. Wang, C., Li, Y., Zhang, C., Chen, X., Liu, C., Weng, W., Shan, W., and He, H. *Appl. Catal., B*, **2021**. 282, 119540.

54. Ran, M., Wang, H., Cui, W., Li, J., Chen, P., Sun, Y., Sheng, J., Zhou, Y., Zhang, Y., and Dong, F. *ACS Appl. Mater. Interfaces*, **2019**. 11, 47984-47991.

55. Wang, B., Liu, J., Yao, S., Liu, F., Li, Y., He, J., Lin, Z., Huang, F., Liu, C., and Wang, M. *J. Mater. Chem. A*, **2021**. 9, 17143-17172.

56. Liu, Z., Tian, J., Yu, C., Fan, Q., and Liu, X. *Chin. J. Catal.*, **2022**. 43, 472-484.

57. Zhang, H., Yang, J., Li, D., Guo, W., Qin, Q., Zhu, L., and Zheng, W. *Appl. Surf. Sci.*, **2014**. 305, 274-280.

58. Schwach, P., Pan, X., and Bao, X. *Chem. Rev.*, **2017**. 117, 8497-8520.

59. Hayyan, M., Hashim, M.A., and AlNashef, I.M. *Chem. Rev.*, **2016**. 116, 3029-85.

60. He, W., Kim, H.K., Wamer, W.G., Melka, D., Callahan, J.H., and Yin, J.J. *J. Am. Chem. Soc.*, **2014**. 136, 750-7.

61. Zhou, W., Qiu, X., Jiang, Y., Fan, Y., Wei, S., Han, D., Niu, L., and Tang, Z. *J. Mater. Chem. A*, **2020**. 8, 13277-13284.

62. Li, Q., Ouyang, Y., Li, H., Wang, L., and Zeng, J. *Angew. Chem. Int. Ed. Engl.*, **2022**. 61, e202108069.

63. Nosaka, Y. and Nosaka, A.Y. *Chem. Rev.*, **2017**. 117, 11302-11336.

64. Song, H., Meng, X., Wang, S., Zhou, W., Song, S., Kako, T., and Ye, J. *ACS Catal.*, **2020**. 10, 14318-14326.